

Magnetic interaction and anisotropy axes arrangement in nanoparticle aggregates can enhance or reduce the effective magnetic anisotropy

V. R. R. Aquino¹, L. C. Figueiredo², J. A. H. Coaquira², M. H. Sousa³, A. F. Bakuzis^{1,*}

¹Instituto de Física, Universidade Federal de Gois, 74690-900, Goinia-GO, Brazil

²Instituto de Física, Nucleo de Física Aplicada, Universidade de Brasília, 70910-900, Brasília-DF, Brazil

³Faculdade de Ceilndia, Universidade de Brasília, 72220-140, Brasília-DF, Brazil

*Corresponding author: bakuzis@ufg.br

Abstract

The magnetic response of nanostructures plays an important role on biomedical applications being strongly influenced by the magnetic anisotropy. In this work we investigate the role of temperature, particle concentration and nanoparticle arrangement forming aggregates in the effective magnetic anisotropy of Mn-Zn ferrite-based nanoparticles. Electron magnetic resonance and coercivity temperature dependence analyses, were critically compared for the estimation of the anisotropy. We found that the temperature dependence of the anisotropy follows the Callen-Callen model, while the symmetry depends on the particle concentration. At low concentration one observes only an uniaxial term, while increasing a cubic contribution has to be added. The effective anisotropy was found to increase the higher the particle concentration on magnetic colloids, as long as the easy axis was at the same direction of the nanoparticle chain. Increasing even further the concentration up to a highly packed condition (powder sample) one observes a decrease of the anisotropy, that was attributed to the random anisotropy axes configuration.

Keywords: magnetic anisotropy, electron magnetic resonance, dipolar interaction, random anisotropy, magnetic hyperthermia.

I INTRODUCTION

The magnetic anisotropy constant have a great impact in the magnetic response of nanoparticles. In non-interacting systems it defines (together with the particle size) if the nanoparticle is at the blocked or superparamagnetic (SP) regime. SP particles are believed to play an important role in biomedical applications, spanning from contrast agents for MRI, heat generators in magnetic hyperthermia, cell sorting applications due to magnetophoresis properties, among others. [1–4] Moreover nanoparticles can form aggregates, for example linv ear chains or spherical nanostructures (even at the SP state due to van der Waals interactions), [5] where in this case the intraparticle interactions (mainly due to magnetic dipolar interactions) can modify the effective magnetic anisotropy. The knowledge of this effect is of great fundamental and technological importance due to the several applications of magnetic nanoparticles (even beyond the biomedical field), since it directly correlates with the relaxation of the magnetization.

In the literature there is still a strong debate about the effect of dipolar interaction, where some authors claim it decreases the effective anisotropy, while others point to the opposite effect. [5–10] It is also curious to notice that few articles discuss about the task of anisotropy axes arrangement, the anisotropy temperature dependence or the particle interaction role on the anisotropy energy symmetry, which again can impact the magnetic relaxation. [11]

Nowadays several techniques are applied to determine the magnetic anisotropy, as for instance ZFC/FC magnetization curves, [12, 13] coercivity temperature dependence analysis, [14, 15] electron magnetic resonance, [16–18] Mossbauer spectroscopy, [6] among others. In some cases one first determine the blocking temperature and then calculate the magnetic anisotropy, where some methods assume the anisotropy to be temperature independent. This is obvious incorrect since several anisotropy contributions are temperature dependent, such as the magnetostatic or magnetoelastic terms. In particular, for the ZFC/FC curves, [12] generally, it is not clear that the determination of anisotropy via blocking temperature is an estimated anisotropy referring to the value at this temperature. For several studies this might not be that important, however there is a great interest on using magnetic nanoparticles for cancer therapy through magnetic hyperthermia. [3, 4, 19, 20] Here temperature effects can have a great impact on the clinical outcome. Furthermore this biomedical application showed a strong dependence upon particle arrangement, [10, 21–26] and therefore understanding the role of particle interactions and nanoparticle arrangements is also crucial. It might also be relevant to notice the experimental condition that the effective anisotropy is determined, for example in some works the magnetic anisotropy of the nanoparticles is estimated using a powder sample, while the relevant application property is analysed for the colloidal suspension. In the powder sample the nanoparticles are highly packed and one might assume that the anisotropy axes are randomly arranged, while in the colloidal suspension distinct aggregate

formations can arise, as for instance linear chains that are expected to have their anisotropy axes arranged along the chain (longitudinal configuration). [27]

In this work, we investigate the role of particle arrangement on the effective magnetic anisotropy by critically comparing data using the coercivity temperature dependence analysis and electron magnetic resonance (EMR). In the H_c vs T method powder samples were analysed, while in the former magnetic colloids at distinct particle concentrations were investigated. Mn-Zn ferrite nanoparticles surface-coated with citric acid of distinct sizes were compared, allowing us to determine the value of the effective magnetic anisotropy from the non-interacting condition (highly diluted magnetic colloid) up to a particle volume fraction of around 0.64, that corresponds to the packing fraction of monodisperse spherical particles. [28] Here, we demonstrate that magnetic anisotropy is strongly temperature dependent, and that its behavior is well represented by the Callen-Callen model. [29] The room temperature anisotropy is found to increase the higher the particle concentration in the colloid, and above a critical concentration it shows a cubic anisotropy symmetry contribution that was not reported before in other works. We show that the experimental result is in accordance with the theoretical prediction that the existence of linear chains will influence the anisotropy by means of an additional uniaxial contribution. [5] On the other hand, the existence of the cubic anisotropy term suggests a multipolar contribution. Increasing even further the concentration up to a highly packed condition (powder sample), we observed a decrease of the anisotropy and relate it to the random anisotropy axes configuration for this particle arrangement situation. The result might be useful on understanding some contradictory reports in the literature regarding the effect of particle interactions, and might impact not only the magnetic hyperthermia field, but also magnetic particle imaging [30,31] and magnetic nanothermometry, [32,33] among others.

The article is organized as follows: In section II, we present the theoretical background for both methods, coercivity temperature dependence analysis and electron magnetic resonance, used to determine the magnetic anisotropy. Different from most works of the literature the effect of the temperature dependence of the anisotropy is explicitly taken into account in the H_c vs T method, that also determines the sample blocking temperature distribution. On the other hand, EMR extracts the anisotropy field. Where from the temperature dependence magnetization studies of the samples one can determine the effective magnetic anisotropy as function of temperature and particle concentration. Section III discuss the experimental procedures, i.e. synthesis and characterization techniques. Finally, section IV presents the results and discussions, while the conclusions are shown in section V.

II THEORETICAL BACKGROUND

A Coercivity temperature dependence method

According to this method, the coercivity temperature dependence $\langle H_C \rangle_T$ of the sample can be modeled using, [34,35]

$$\langle H_C \rangle_T = \frac{M_R(T)}{\chi_{sp}(T) + \frac{M_R(T)}{H_{CB}(T)}}, \quad (1)$$

where $M_R = \alpha M_s \int_T^\infty P(T_{Bl}) dT_{Bl}$ is the remanent magnetization, $\chi_{sp} = \frac{25M_s^2}{3K_{ef}} \int_0^T T_{Bl} P(T_{Bl}) dT_{Bl}$ the superparamagnetic susceptibility, $P(T_{Bl})$ is the lognormal distribution function of the blocking temperatures (T_{Bl}). For randomly oriented particle systems $\alpha = 0.48$, while H_{CB} is described by the following equation

$$H_{CB}(T) = \alpha \frac{2K_{ef}(T)}{M_s} \left(1 - \left(\frac{T}{\langle T_{Bl} \rangle_T} \right)^{3/4} \right), \quad (2)$$

with $\langle T_{Bl} \rangle_T = \frac{\int_T^\infty T_{Bl} P(T_{Bl}) dT_{Bl}}{\int_T^\infty P(T_{Bl}) dT_{Bl}}$ a temperature dependent parameter related to the distribution of the blocking temperatures at a given temperature T , while the exponent 3/4 corresponds to the random anisotropy case. [35] More important, different from previous works in the literature, the effective anisotropy constant is assumed to be temperature dependent. This dependence is shown to experimentally follow the Callen-Callen model, [29] which establishes a relationship between magnetization and anisotropy via the equation:

$$\frac{K(T)}{K(0)} = \left[\frac{M_s(T)}{M_s(0)} \right]^{l(l+2)/2}, \quad (3)$$

For the uniaxial case $l = 2$ and $K(0)$ is the anisotropy at $T = 0 K$. Thus, this equation can be rewritten using the Bloch model, $M_s(T) = M_s(0) (1 - bT^{3/2})$, where $M_s(0)$ is the saturation magnetization at $0 K$ and b is the Bloch constant, that are determined from magnetization measurements. Therefore, the temperature dependence of the effective uniaxial magnetic anisotropy constant can be written as

$$K_{ef}(T) = K(0) \left(1 - bT^{3/2} \right)^3. \quad (4)$$

B EMR method

The other technique that will be used to estimate the magnetic anisotropy is the Electron Magnetic Resonance (EMR). For spherical particles the resonance field condition is given by [16, 17]

$$H_R = \frac{\omega}{\gamma\sqrt{1-\alpha^2}} - \frac{2K_{ef}}{M_S}, \quad (5)$$

where ω is the angular frequency, γ is the gyromagnetic ratio and α is the damping term (usually much lower than 1). Note that the effective anisotropy constant can be expanded in terms of spherical harmonics such as $K_{ef} = \sum_l \sum_m K_l P_l(\cos\theta) e^{im\varphi}$, where P_l is the Legendre polynomial and θ is the angle between the applied magnetic field and the nanoparticle anisotropy axis. [16] For spherical particles, $m = 0$, while considering only the uniaxial case, $l = 2$ term, reveals an uniaxial anisotropy field $2K_2^s/M_S P_2(\cos\theta)$. For the longitudinal case ($\theta = 0$) this expression is the well known uniaxial anisotropy field $2K_2^s/M_S$, as expected. On the other hand, more complex cases can appear by including other values of l , that reflect the symmetry of the anisotropy. For example, the additional existence of a cubic contribution, $l = 4$, results in the condition:

$$H_R = \frac{\omega}{\gamma\sqrt{1-\alpha^2}} - \frac{2K_2}{M_S} P_2(\cos\theta) - \frac{2K_4}{M_S} P_4(\cos\theta). \quad (6)$$

So, the behavior of Hr as a function of the angle can indicate the anisotropy symmetry, where including only the $l = 2$ term, reflects an uniaxial anisotropy symmetry, while the necessity of other contributions reveals a more complex situation.

C Dipolar interaction contribution to the anisotropy

In 2013, Bakuzis et al. [5] mathematically showed that the dipolar interaction between nanoparticles, forming small agglomerates in a linear chain, has a uniaxial contribution due to the particle-particle interaction term. The linear chain model was applied to two situations, namely fanning and coherent. In the coherent case, it is assumed that the magnetic moments of the particles are all in the same direction, rotating coherently in the direction of the magnetic field. In the fanning structure, the magnetic moments of the adjacent particles rotate in opposite directions. In both cases, fanning and coherent, a uniaxial contribution to the energy density of the particle ($l = 2$ term) is noted. [5] These results can be generalized for the case of a chain containing Q particles. Below, we present the contribution to effective anisotropy constant in the fanning case, [5, 10]

$$K_{dip}^{fanning} = \frac{\mu_0}{4\pi} \frac{M_S^2 V_P}{(\bar{D} + d_{ss})^3} \times \left(\sum_{i=odd}^Q \frac{(Q-i)}{Q(i)^3} + 3 \sum_{i=pair}^Q \frac{(Q-i)}{Q(i)^3} \right),$$

where μ_0 is a magnetic permeability of the vacuum, \bar{D} is the nanoparticles mean diameter and V_P the particle volume. The nanoparticles centers are distant from a value $r = \bar{D} + d_{ss}$, where d_{ss} is the distance between the surfaces of the nanoparticles. The coherent calculation can be found in. [5]

III EXPERIMENTAL PROCEDURE

Among the various methods for synthesizing magnetic nanoparticles, with new morphologies and dimensions, the hydrothermal technique has been extensively explored. This synthetic route allows working with temperatures above the boiling point of the chosen solvent, changing the crystallization/recrystallization conditions in the synthetic environment. [36] For the preparation of magnetic nanoparticles based on manganese-zinc ferrite with the stoichiometry $Mn_{0.75}Zn_{0.25}Fe_2O_4$, we mixed 3.75 mmol of manganese chloride tetrahydrate ($MnCl_2 \cdot 4H_2O$), 1.25 mmol of ions zinc chloride ($ZnCl_2$) and 10 mmol of ferric chloride hexahydrate ($FeCl_3 \cdot 6H_2O$) from 1 mol/l stock solutions. Thus, 50 ml of 8.0 wt% aqueous methylamine (CH_3NH_2) was poured into the metal's solution under magnetic stirring for about 5 min at room temperature. The mixture was sealed in a teflon-lined autoclave and maintained at 160 °C for 5 h inside an oven.

After this time, the formed magnetic material was washed three times with distilled water. To the resulting magnetic material was added 300 ml To prepare the citrate-capped nanoparticles, 2 g of trisodium citrate was added to this dispersion under magnetic stirring at 80 °C for 30 minutes. The precipitate was magnetically separated, washed with acetone and redispersed in water. The pH of dispersion was carefully adjusted to form a stable magnetic fluid at pH ~ 7 . To obtain samples with different mean diameters, we used a size-sorting method based on the increase the ionic strength of the sol – through the addition of NaCl – which induces a phase transition in the colloid. [37, 38] Typically, NaCl is added to the sol with a magnet placed at the bottom of the flask until visual colloidal separation. After magnetic separation, the supernatant (with smallest nanoparticles) and precipitate (with larger nanoparticles) are washed with acetone in order to resuspend nanoparticles in aqueous solution at pH ~ 7 .

Once the magnetic fluid was achieved, they were diluted in different volume fractions, which were checked by expression: $\phi \approx M_{fluid}/M_s$, where M_{fluid} and M_s are the saturation magnetization of the fluid and the powder, using a VSM (vibrating sample magnetometer, *2 Tesla*). After obtaining the magnetic fluid, the nanoparticles were characterized by several techniques, such as energy dispersive spectroscopy (EDS), obtaining images for compositional analysis; X-ray diffraction (XRD), to obtain the crystalline phase and the average size of the crystallite; transmission electron microscopy (TEM), for the calculation of the distribution of diameters and shape of the particles; Superconducting Quantum Interference Device (SQUID) magnetometer, necessary to achieve saturation magnetization and the coercive field at low temperatures and electron magnetic resonance (EMR), for anisotropy field determination.

Measurements of the chemical composition of the samples were carried out using energy dispersive spectroscopy (EDS) using the transmission electron microscope (JEOL model JEM-2100), operating in EDS mode at 15 kV. For the determination of particle sizes, we dry a part of the colloid to obtain the powder and perform the analysis by XRD (Shimadzu 6000). Images of the nanoparticles were obtained using the transmission electron microscope (Jeol model JEM-2100) operated at 200 kV, with resolution of 25 Å. For the characterization of magnetic properties at low temperatures, we used a VSM-SQUID (Quantum Design PPMS3) with a DC field ranging from -70 to 70 kOe, and temperatures ranging from 5 to 300 K. On the other hand the calculation of the particle volume fraction at room temperature was obtained using a VSM (ADE Magnetic, EV-9 model) with a DC field ranging from -20 to 20 kOe. Finally, EMR measurements were performed with a spectrometer EMX-Plus model Bruker, where the magnet had a magnetic field amplitude up to 14 kG and X-band microwave bridge tuned around 9.5GHz. The EMR procedure to extract the anisotropy field was the same of Refs. [16, 17, 39]. Basically, at room temperature, one apply the highest external magnetic field to the magnetic fluid sample with the objective to orient the nanoparticle magnetic anisotropy axis along the field direction. With the field on, the sample is frozen to 100K. The procedure blocks the nanoparticle's anisotropy in a specific direction. A goniometer device allow rotation of the sample with respect to the applied field during the EMR experiment. So, EMR spectra at distinct angles, for a given temperature and particle concentration, can be obtained to determine the value and symmetry of the effective anisotropy constant.

IV RESULTS AND DISCUSSION

Figure 1(a) shows the XRD data for both nanoparticles confirming the cubic spinel structure. Crystallite sizes of 10.3 and 11.4 nm were obtained using the Scherrer equation, i.e. $D_{XRD} = \kappa\lambda/\beta\cos\psi$, where $\kappa = 0.89$ is the Scherrer constant, $\lambda = 0.154$ nm is the X-ray wavelength, β is the line broadening in radians obtained from the square root of the difference between the square of the experimental width of the most intense peak to the square of silicon width (calibration material), and ψ is the Bragg angle of the most intense peak. The inset of Fig. 1(b) shows an image of a film made of 10 nm nanoparticles, while some spots show places where were performed the EDS-TEM analysis. Fig. 1b shows the EDS analysis of this sample, where one can clearly observe the existence of Mn, Zn and Fe, as expected (Cu signal is due to the TEM microgrids). Fig 1(c) shows the size distribution for both samples obtained from the analysis of TEM pictures, while the inset shows TEM images of the 10nm size nanoparticles revealing spherical-like particles. From the fit of the histogram using the lognormal distribution size (median and size dispersion parameters) one can calculate the mean diameters and the standard deviation, 10 ± 2 and 11 ± 2 nm. Magnetic characterization is shown in Figure 1(d) for the 10nm particle size, while the inset shows hysteresis curves at low field range. Measurements were performed at a wide temperature range 5 to 300 K for a powder sample. The saturation magnetization value is obtained from the analysis at the high field limit, i.e. from extrapolation of data of $M \times 1/H$ when $1/H$ tends to zero. Fig. 1(e) shows the temperature dependence of the saturation magnetization for both samples. The symbols represent the experimental data, while line is the best fit using the Bloch's law, that revealed the Bloch constants, 7.5×10^{-5} and $6.6 \times 10^{-5} K^{-3/2}$ for 10 and 11 nm diameters and the saturation magnetization value at 0 K, 585 and 565 emu/cm^3 , respectively. On the other hand, the particle concentration of the magnetic fluids was obtained by the analysis of the magnetization at room temperature using a 2T VSM. Figure 1(f) shows the magnetization curves of the same sample but now at different particle volume fractions (ϕ). The estimation of ϕ arises from the ratio of the saturation magnetization of the sample to the saturation measured for the nanoparticle (powder sample) at the same experimental condition, that for our samples were found to be 293 emu/cm^3 and 303 emu/cm^3 for particles of 10 and 11 nm.

A Blocking temperature distribution

Figure 2(a) shows the temperature dependence of the coercivity for both samples, while in the inset is shown the low field hysteresis curves for the 11nm sample. Symbols correspond to experimental data, while the lines correspond to the best fit using the theoretical model discussed in section IIA, that included the effective anisotropy temperature dependence by using $K_{ef}(T) = K(0) (1 - bT^{3/2})^3$. It is clear in this model that only the value of the anisotropy at 0 K becomes one of the parameters of adjustment of the coercive field data, where the other fitting parameter is related to the blocking temperature distribution, T_{Bl}^m . Note that because of lognormal distribution properties, one can assume that the dispersion of blocking temperatures (that is proportional to the particle volume) is related to

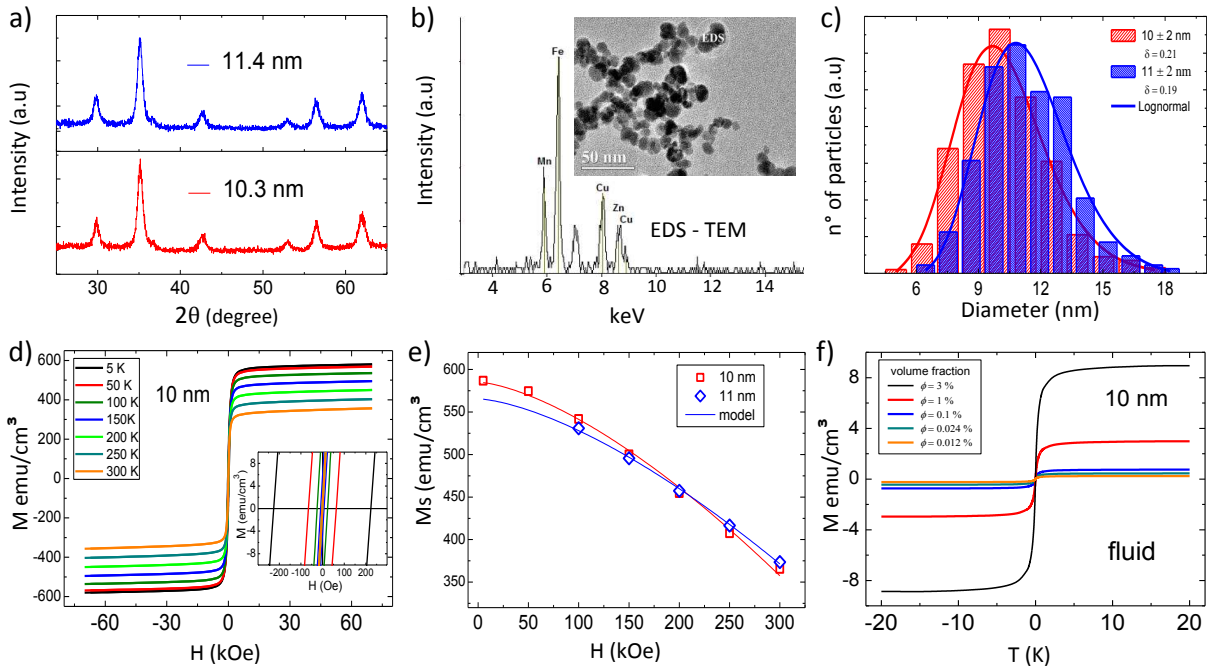


Figure 1: (a) XRD data of the MnZn samples. Crystalline sizes are determined using Scherrer equation. (b) EDS analysis of the 10nm sample showing the existence of Mn, Zn and Fe in the nanoparticle composition. The inset shows a TEM picture and the position of the EDS analysis. (c) Size distribution obtained by TEM. (d) Hysteresis curves at distinct temperatures for the 10nm sample. The inset shows the magnetization curves at low field range. (e) Saturation magnetization temperature dependence study. Symbols represent data, while lines are the Bloch law model. (f) Magnetization data of the 10nm-based colloid for particle volume fraction determination.

Table 1: Effective anisotropy constants and average blocking temperatures of the $\text{Mn}_{0.75}\text{Zn}_{0.25}\text{Fe}_2\text{O}_4$ samples according to the coercivity temperature dependence analysis.

\bar{D} (nm)	K_{ef}^n (erg/cm ³)	\bar{T}_{Bl}^n (K)	$K_{ef}(0\text{ K})$ (erg/cm ³)	$K_{ef}(300\text{ K})$ (erg/cm ³)	\bar{T}_{Bl} (K)
10	1.5×10^5	110 ± 76	1.5×10^5	3.4×10^5	122 ± 85
11	1.4×10^5	130 ± 80	1.4×10^5	4.1×10^4	141 ± 87

the size dispersity (obtained from TEM analysis) through $\sigma_B = 3\sigma_{TEM}$. Therefore, the mean blocking temperature of the sample can be calculated using the equation $\bar{T}_{Bl} = T_{Bl}^m \exp[(\sigma_B)^2/2]$. Fig 2(b) shows the blocking temperature distribution obtained from the analysis of $\langle Hc \rangle_T$ vs T . The dashed lines indicate the position of the mean blocking temperature for both samples. As expected, higher value was found for the larger particle size.

Table 1 summarizes the parameters obtained from the coercive field analysis, $\langle Hc \rangle_T$ vs T method, namely \bar{T}_{Bl} and $K_{ef}(0\text{ K})$. For comparison we also included the values estimated using the non-temperature dependent model, K_{ef}^n and \bar{T}_{Bl}^n . Curiously the value obtained is very close to $K_{ef}(0\text{ K})$, while \bar{T}_{Bl}^n is slightly lower than \bar{T}_{Bl} . As for instance, the 10nm sample showed $\bar{T}_{Bl} = 122\text{K}$, while for the non-temperature dependent model $\bar{T}_{Bl}^n = 110\text{K}$. The difference with other models from the literature [34] are that: (i) firstly, in our case, we can easily identify the temperature correspondence of this anisotropy; (ii) Second, here there is no necessity to fit ZFC/FC curves to extract the blocking temperature distribution, a procedure that depending on the nanoparticle is not easily performed; (iii) In the present model, one can estimate the anisotropy constant at room temperature, where it is found that both samples shows room temperature anisotropy values on the order of $\sim 10^4$ erg/cm³. However, it is very important to notice that so far we made the assumption that the anisotropy temperature dependence follows the Callen-Callen model. In the next section we demonstrate that this is indeed a very good approximation.

B Anisotropy temperature dependence and the Callen-Callen model

The inset of Fig. 2(c) shows EMR spectrum at different angle positions for the 10nm sample with a particle volume fraction of 3%. Similar experiments were performed at distinct particle concentrations for both samples. Fig. 2(c) shows the resonance field position as function of the angle between the applied field and the anisotropy axis for the

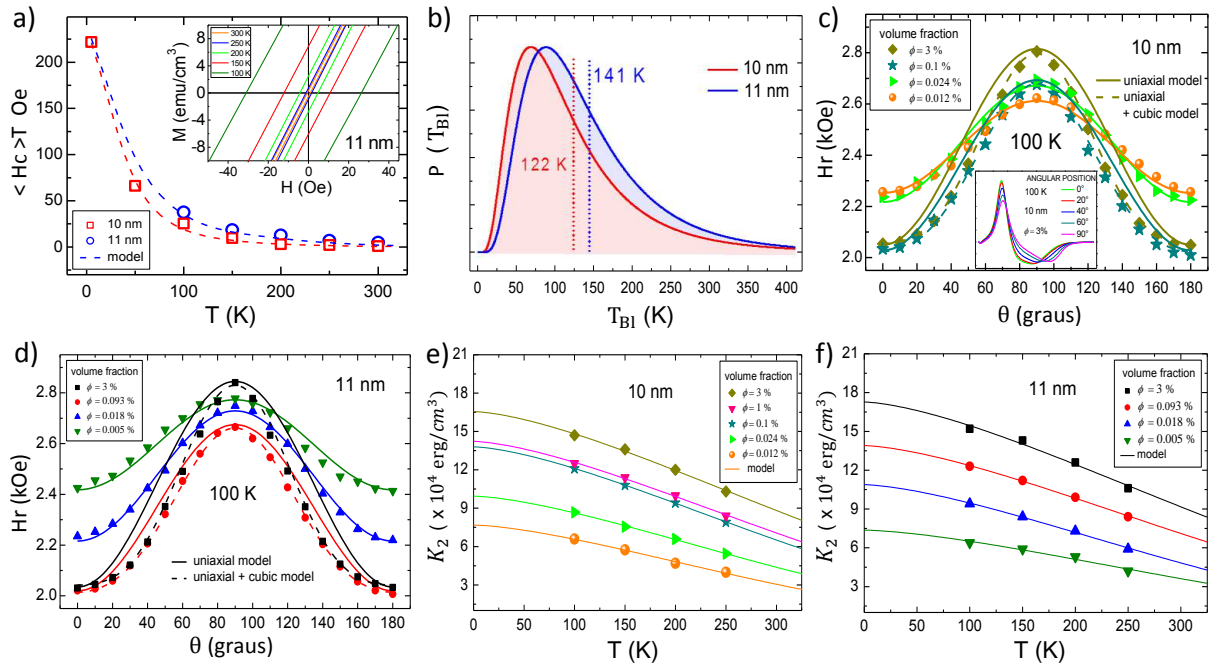


Figure 2: (a) Coercive field as function of temperature. Symbols are data, while lines correspond to the model. The inset shows the magnetization curves at low field range for the 11nm sample. (b) Blocking temperature distributions obtained from the model for both samples. In (c) and (d) EMR field as function of the angle between the applied field and the anisotropy axis at 100K and distinct particle concentrations, respectively for the 10nm and 11nm samples. Solid and dash lines are the adjustments of the experimental data according to the models discussed in the text. The inset in (c) shows typical EMR spectra at distinct angles. In (e) and (f) symbols represent the uniaxial anisotropy term K_2 as function of temperature and particle concentration, respectively for 10 and 11nm samples, while lines are the best fit using the Callen-Callen model.

10nm sample at different particle concentrations, while Fig. 2(d) shows similar data but for the 11nm sample. It is clear that there is a shift in the resonance field position increasing the angle up to 90 degrees. Above this value the resonance field position decreases returning to its initial position for an angle of 180 degrees. The EMR measurements shown here were performed at 100 K, but other experiments at temperatures 150, 200 and 250K were also obtained. Higher temperatures were not analysed because the nanoparticles were dispersed in water, and we wanted to maintain the nanoparticles in the frozen matrix and avoid the solid-liquid transition. Symbols represent EMR data, while solid lines corresponds to the uniaxial case (only $l = 2$ term - K_2^s) and dashed lines are the multiaxial case (Eq.(6)), where one can obtain the values of K_2 and K_4 . Note that, for low concentrations, the uniaxial contribution alone (K_2^s) is able to explain the behavior of the resonance field. In particular, it is further noted that the increase in the difference of the Hr variation is a result of a higher anisotropy when the concentration increases. However, in the higher concentrations the adjustment of the experimental data considering only the $l = 2$ term was not so good. Therefore the analysis presented here corresponds to the one using Eq. (6), i.e. one obtain both K_2 and K_4 . According to the theoretical models the difference between the resonance field at 0 and 90 degrees is related to the anisotropy field. Since the saturation magnetization temperature dependence was determined before (see Fig. 1(e)), using the anisotropy field we extract the temperature dependence of the anisotropy constants. Figs. 2(e) and 2(f) shows the effective anisotropy temperature dependence for the 10 and 11 nm samples, respectively. Here we are showing only the K_2 value, but Table 2 summarizes all the other parameters analysed in this study (including the K_2^s for the uniaxial case). Symbols represent experimental data, while solid lines correspond to the best fit using the Callen-Callen model. It is obvious from this analysis the excellent agreement with the data, justifying the assumption on the later section. On the other hand, K_4 is only relevant at high particle concentrations, although its value is around one order of magnitude lower than K_2 (see Table 2). Room temperature anisotropy values can be found using the Callen-Callen model, and revealed an increase the higher the particle concentration. Above a critical concentration a cubic anisotropy symmetry contribution has to be added in the analysis, suggesting a possible multipolar contribution to the anisotropy. Possibly, this is the first experimental evidence of the existence of a multipolar contribution at high concentrations. It is possible that such term is the result of a more complex organization of nanoparticles than only isolated linear chains. In favor of this argument is the fact, well known in the literature, that the magnetic fluid has a liquid-solid transition increasing the concentration of particles. [40, 41] This phenomenon results in the formation of complex self-organized structures, for example in the formation of hexagonal columnar structures. [41] This might be different from the case of isolated linear chains, that due to the dipolar interaction between nanoparticles showed only a uniaxial contribution term. [5]

Table 2: Anisotropy constants of $\text{Mn}_{0.75}\text{Zn}_{0.25}\text{Fe}_2\text{O}_4$ of 10 and 11nm for each concentration and at different temperatures. Thus, from 100 to 250 K EMR data, while 0 and 300 K corresponds to extrapolation values using Callen-Callen model.

ϕ	\bar{D}	0 K			100 K			150 K			200 K			250 K			300 K	
		K_2	$-K_4$	K_2^s	K_2	$-K_4$	K_2^s	K_2	$-K_4$	K_2^s	K_2	$-K_4$	K_2^s	K_2	$-K_4$	K_2^s	K_2	$-K_4$
(%)	(nm)	$(\times 10^4 \text{erg/cm}^3)$			$(\times 10^4 \text{erg/cm}^3)$			$(\times 10^4 \text{erg/cm}^3)$			$(\times 10^4 \text{erg/cm}^3)$			$(\times 10^4 \text{erg/cm}^3)$			$(\times 10^4 \text{erg/cm}^3)$	
3	10	16.5			14.7	3.3	13.8	13.6	3.0	12.8	12.0	2.6	11.2	10.3	2.3	9.6	8.8	1.70
1	10	14.2			12.5	2.2	11.3	11.4	2.3	10.5	10.0	1.8	9.1	8.4	2.3	7.9	7.1	1.19
0.1	10	13.8			12.1	2.1	10.6	10.8	1.8	9.8	9.4	1.3	8.7	7.9	1.1	7.6	6.5	0.98
0.024	10	9.9			8.7	1.0	8.4	7.6	0.8	7.1	6.6	0.8	6.4	5.4	0.6	5.4	4.4	0.46
0.012	10	7.8			6.6	0.3	6.5	5.7	0.2	5.6	4.7	0.3	4.8	4.0	0.3	3.9	3.2	0.22
3	11	17.3			15.2	3.6	14.6	14.3	3.3	13.3	12.6	2.7	12.0	10.6	2.2	10.1	9.5	1.77
0.093	11	13.9			12.2	1.9	14.6	11.2	1.7	10.6	9.9	1.4	9.5	8.3	1.0	8.2	7.2	0.76
0.018	11	10.9			9.4	0.8	9.1	8.4	0.6	7.9	7.3	0.4	7.1	5.9	0.2	5.8	4.9	0.13
0.005	11	7.5			6.4	0.3	6.5	5.9	0.2	5.8	5.3	0.1	5.1	4.2	0.1	4.1	3.6	0.04

C The role of the magnetic interaction and axes arrangement on the anisotropy

The excellent agreement between the experimental data and the Callen-Callen model allowed us to calculate the anisotropy constants by extrapolation at 0 K and 300 K for both samples. Table 2 summarizes all the results obtained as function of temperature and concentration. Also, since the main anisotropy contribution arises from the uniaxial term for most samples, from now on we will focus on the room temperature concentration dependence of K_2 . Figure 3(a), presents the data at the ambient temperature of the effective anisotropy constant (considering only the uniaxial term - K_2), for different samples, as a function of the particle volume fraction. Open symbols corresponds to the analysis obtained from the EMR data of the colloids, while solid symbols correspond to the coercivity temperature dependence analysis (of the powder). According to the literature, [28] for monodisperse spherical nanoparticles one can assume that the packing of the nanoparticles in the powder configuration corresponds to a particle volume fraction close to $\phi = 0.64$ (although the nanoparticles are not perfectly spherical or monodisperse this is considered to be a good approximation). Recall that unlike the case of the magnetic fluid in which the anisotropic axes are oriented towards the freezing field (longitudinal case [27]), in the case of the powdered sample the axes are estimated to be in the random configuration. For the colloid one can observe an increase of the effective magnetic anisotropy the higher the particle concentration. This result is in agreement with the theoretical prediction for the case of nanoparticles forming a linear chain. [5]

On the other hand, for the higher concentration, a lower value is observed for the anisotropy, which at first can suggest the existence of a maximum as a function of the concentration. Indeed, the random anisotropy model, already applied even for magnetic dipolar fluids, [42] suggests a decrease of the effective anisotropy, such that for the case of N particles interacting collectively, the anisotropy can be represented as $K_{ef} = K_{int}/\sqrt{N}$. Here K_{int} refers to the anisotropy of an individual particle (interacting or non interacting). Therefore, the transition from a longitudinal to random condition may explain such a decrease, at least qualitatively. As discussed previously, to explain the existence of the cubic term in the anisotropy, it is known in magnetic fluids that increasing the concentration of particles occurs a liquid-solid transition. [40,41] In this case, formation of complex self-organized structures can break the longitudinal condition, favoring a situation with randomly organized anisotropy axes. The consequence of such an effect may be the decrease in anisotropy. In the case of samples of magnetic fluids such an effect was not observed, but may appear only in the case of higher concentrations, which would allow the existence of a maximum. As this did not happen for the fluids in our experimental condition, we decided to theoretically determine, via the linear chain model, [5] if the increase in the size of the chain is able to explain the value of the anisotropy observed experimentally.

Figure 3(b) presents the calculations of the increase of the effective magnetic anisotropy for a 11nm nanoparticle of $Mn_{0.75}Zn_{0.25}Fe_2O_4$, for fanning (squares) and coherent (circles) cases, assuming a surface-to-surface distance of 1.1nm (estimated for citric acid molecules). An increase in the effective anisotropy of the nanoparticle is clearly evident with the increase in the number of particles in the chain. It is also observed the effective anisotropy value tends to saturation for a large number of particles in the chain, being higher for the coherent case. The role of particle size is shown in the inset of Fig. 3(c) considering only the fanning case. From the theoretical estimations of Fig. 2(b), by comparison with the values extracted from the EMR analysis, it is possible to estimate the chain size for any magnetic particle concentration of the colloids. For example, for $\phi = 0.03$ we found an anisotropy value of $K_{ef} = 9.5 \times 10^4 \text{ erg/cm}^3$ that for the fanning case reveals a mean chain size of 5.3. The arrows indicate the average chain size (x-axis) that has the experimental value of the anisotropy (y-axis). Thus, for the volumes fractions of 0.005, 0.018, 0.093 and 3 %, we obtain as average: 1.1, 1.5, 2.8 and 5.3 particles in a chain for the case fanning and 1.0, 1.1, 1.3 and 1.6 particles for the coherent case, in which it is clear the increase of the size of the aggregate as a function of the concentration of particles. Further smaller chains are observed for the coherent case when compared to the fanning system. It is known, however, that in the situation of lower energy the fanning case is more favorable. Figure 3(c) shows the increase in the number of aggregates with the increase of the particle volume fraction for both samples, considering the fanning case. Similar trend is found for both particle sizes and suggest that the increase in the effective magnetic anisotropy is related to the formation of larger linear chains the higher the particle concentration. This behavior is in accordance with the theoretical model of Refs. [5, 10] that states an increase of the effective anisotropy due to the dipole-dipole particle interaction.

Finally, it is tempted to discuss what are the implications of for cancer hyperthermia. Firstly, if the heat generation is governed by the Nel relaxation mechanism, then is obvious that the results presented here have important consequences, since the relaxation magnetization depends exponentially on the effective anisotropy. So, one could in principle tune the effective anisotropy in order to maximize the heat generation. If one needs to increase the anisotropy then linear chains are interesting options. Indeed, magneto-bacteria chains have been shown to heat efficiently at high field conditions. On the other hand, if one needs to decrease the effective anisotropy, then arranging the nanoparticles as spherical aggregates seems an interesting approach because the random anisotropy axes configuration could lead to this goal. Behind this effect one can find the explanation for several apparently contradictory results regarding the role of the magnetic particle interaction on the heat efficiency.

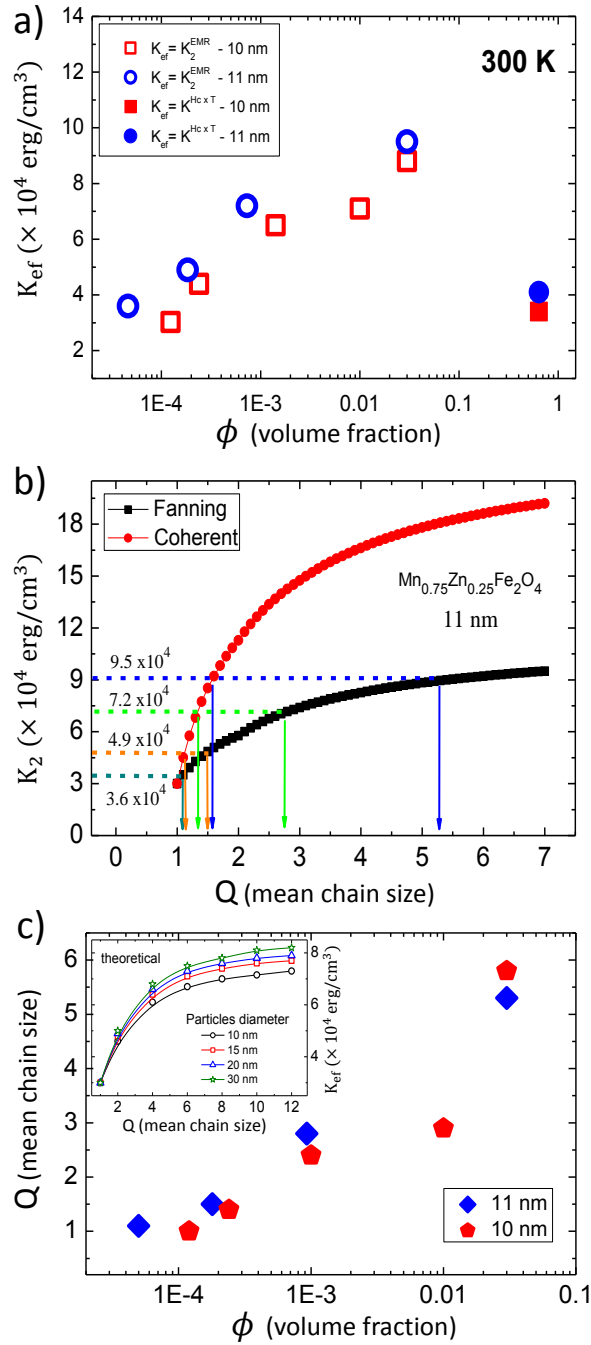


Figure 3: (a) Room temperature uniaxial anisotropy constant as function of particle volume fraction for both samples. Open symbols corresponds to dat obtained by *EMR* method, while solid symbols are obtained from the *Hc vs T* method. (b) Theoretical anisotropy constant calculation as function of chain size. Circles corresponds to coherent, while squares are the fanning case. Here we used $d_{ss} = 1.1 \text{ nm}$ and $M_s = 366 \text{ emu/cm}^3$. Arrows indicate the chain size corresponding to the experimental effective anisotropy value (dash lines). (c) Mean chain size as function of particle volume fraction for both samples assuming the fanning case. The inset shows the same as (b) for the fanning case, but including distinct particle sizes.

V CONCLUSION

Electron magnetic resonance analysis showed that the anisotropy field of these nanoparticles at low particle concentration show uniaxial symmetry that grows with increasing particle volume fraction, thus confirming the influence of the dipole-dipole interaction. At very high particle concentrations, a cubic symmetry term for the anisotropy has to be added to the model suggesting the possibility of multipolar contributions. It was also possible to prove that the anisotropy of these nanoparticles is strongly temperature dependent, and can be adjusted with the Callen-Callen model. The room-temperature magnetic anisotropy values obtained from EMR data analysis for the $\text{Mn}_{0.75}\text{Zn}_{0.25}\text{Fe}_2\text{O}_4$ based colloids as a function of the concentration were the linear chain model with anisotropy axes aligned in the chain direction, longitudinal configuration. This analysis indicates that the increase of the anisotropy with the concentration is related to the existence (and formation) of chains in the magnetic colloid, and that the size of them increases with the concentration. In particular, for the 11 nm sample the anisotropy changed from $3.6 \times 10^4 \text{ erg/cm}^3$, corresponding to an average chain size of only 1.1 for the most dilute case, to an anisotropy value of $9.5 \times 10^4 \text{ erg/cm}^3$, which in the model corresponds to a chain containing on average 5.3 for the most concentrated sample (3% volume fraction). On the other hand, the anisotropy of the powder sample (estimated to have a particle volume fraction around 64%), that was evaluated from the coercive field temperature dependence analysis, showed a reduction of the anisotropy to $4.1 \times 10^4 \text{ erg/cm}^3$, probably due to the random distribution of the anisotropy axes in this experimental condition. The results indicate that the effective magnetic anisotropy is strongly dependent on the magnetic interaction between the particles and the arrangement of the anisotropy axes, which might explain some contradictory discussions in the literature since one might enhance or decrease the effective anisotropy depending on the specific situation.

ACKNOWLEDGMENTS

The authors would like to thank financial support from the Brazilian agencies CNPq, CAPES, FAPEG, FAPDF and FUNAPE.

References

- [1] Y. Javed, K. Akhtar, H. Anwar, and Y. Jamil. Mri based on iron oxide nanoparticles contrast agents: effect of oxidation state and architecture. *Journal of Nanoparticle Research*, 19:366, 2017.
- [2] Z. R. Stephen, F. M. Kievit, and M. Zhang. Magnetite nanoparticles for medical mr imaging. *Materials Today*, 14:330 – 338, 2011.
- [3] B. T. Mai, P. B. Balakrishnan, M. J. Barthel, F. Piccardi, D. Niculaes, F. Marinaro, S. Fernandes, A. Curcio, H. Kakwere, G. Autret, R. Cingolani, F. Gazeau, and T. Pellegrino. Thermoresponsive iron oxide nanocubes for an effective clinical translation of magnetic hyperthermia and heat-mediated chemotherapy. *ACS Applied Materials & Interfaces*, 2019.
- [4] H. F. Rodrigues, F. M. Mello, L. C. Branquinho, N. Zufelato, E. P. Silveira-Lacerda, and A. F. Bakuzis. Real-time infrared thermography detection of magnetic nanoparticle hyperthermia in a murine model under a non-uniform field configuration. *International Journal of Hyperthermia*, 29(8):752–767, 2013.
- [5] A. F. Bakuzis, L. C. Branquinho, L. L. Castro, M. T. A. Eloi, and R. Miotto. Chain formation and aging process in biocompatible polydisperse ferrofluids: Experimental investigation and monte carlo simulations. *Adv. Colloid Interface Sci.*, 191-192:1–21, 2013.
- [6] S. Mørup and E. Tronc. Superparamagnetic relaxation of weakly interacting particles. *Phys. Rev. Lett.*, 72:3278–3281, 1994.
- [7] F. Bødker, S. Mørup, and S. Linderøth. Surface effects in metallic iron nanoparticles. *Physical Review Letters*, 72(2):282–285, 1994.
- [8] J L Dormann, L Bessais, and D Fiorani. A dynamic study of small interacting particles: superparamagnetic model and spin-glass laws. *Journal of Physics C: Solid State Physics*, 21:2015–2034, 1988.
- [9] J L. Dormann, Franco D’Orazio, F Lucari, E Tronc, P Pren, J P. Jolivet, D Fiorani, R Cherkaoui, and M Nogués. Thermal variation of the relaxation time of the magnetic moment of fe2o3 nanoparticles with interparticle interactions of various strengths. *Physical review. B, Condensed matter*, 53:14291–14297, 1996.
- [10] L. C. Branquinho, M. S. Carrião, A. S. Costa, N. Zufelato, M. H. Sousa, R. Miotto, R. Ivkov, and A. F. Bakuzis. Effect of magnetic dipolar interactions on nanoparticle heating efficiency: Implications for cancer hyperthermia. *Scientific Reports*, 3:2887, 2013.

- [11] W. T. Coffey and Y. P. Kalmykov. Thermal fluctuations of magnetic nanoparticles: fifty years after brown. *Journal of Applied Physics*, 112:121301, 2012.
- [12] M. Knobel, W. C. Nunes, L. M. Socolovsky, E. De Biasi, J. M. Vargas, and J. C. Denardin. Superparamagnetism and other magnetic features in granular materials: a review on ideal and real systems. *J. Nanosci. Nanotechnol.*, 8(6):2836–2857, 2008.
- [13] F Zeb, M Ishaque, K Nadeem, M Kamran, H Krenn, and D V Szabo. Surface effects and spin glass state in co3o4 coated MnFe2o4 nanoparticles. *Materials Research Express*, 5:086109, 2018.
- [14] J. C. Denardin, A. L. Brandl, M. Knobel, P. Panissod, A. B. Pakhomov, H. Liu, and X. X. Zhang. Thermoremanence and zero-field-cooled/field-cooled magnetization study of co(sio2)1-x granular films. *Phys. Rev. B.*, 65:064422, 2002.
- [15] E. Mendona, C B. R. Jesus, W. Folly, C. Meneses, J Duque, and A A. Coelho. Temperature dependence of coercive field of znfe2o4 nanoparticles. *J. Appl. Phys.*, 111:053917, 2012.
- [16] A. F. Bakuzis, P. C. Morais, and F. A. Tourinho. Investigation of the magnetic anisotropy in manganese ferrite nanoparticles using magnetic resonance. *Journal of Magnetic Resonance*, 122:100–103, 1996.
- [17] A. F. Bakuzis, P. C. Morais, and F. Pelegrini. Surface and exchange anisotropy fields in $MnFe_2O_4$ nanoparticles: Size and temperature effects. *Journal of Applied Physics*, 85(10):7480–7482, 1999.
- [18] F Gazeau, J.C Bacri, F Gendron, R Perzynski, Yu.L Raikher, V.I Stepanov, and E Dubois. Magnetic resonance of ferrite nanoparticles:: evidence of surface effects. *J. Magn. Magn. Mater.*, 186(1):175 – 187, 1998.
- [19] A. Jordan, R. Scholz, P. Wust, H. Fhling, J. Krause, W. Wlodarczyk, B. Sander, Th. Vogl, and R. Felix. Effects of magnetic fluid hyperthermia (mfh) on c3h mammary carcinoma in vivo. *Int. J. Hyperthermia*, 13:587–605, 1997.
- [20] H. F. Rodrigues, G. Capistrano, F. M. Mello, N. Zufelato, E. Silveira-Lacerda, and A. F Bakuzis. Precise determination of the heat delivery duringin vivomagnetic nanoparticle hyperthermia with infrared thermography. *Physics in Medicine and Biology*, 62:4062–4082, 2017.
- [21] C. L. Dennis, K. L. Krycka, J. A. Borchers, R. D. Desautels, J. van Lierop, N. F. Huls, A. J. Jackson, C. Gruettner, and R. Ivkov. Internal magnetic structure of nanoparticles dominates time-dependent relaxation processes in a magnetic field. *Advanced Functional Materials*, 25(27):4300–4311, 2015.
- [22] S. Jeon, K. R Hurley, J. C. Bischof, C. Haynes, and C. Hogan. Quantifying intra- and extracellular aggregation of iron oxide nanoparticles and its influence on specific absorption rate. *Nanoscale*, 8:16053, 2016.
- [23] M. L. Etheridge, K. R. Hurley, J. Zhang, S. Jeon, H. L. Ring, C. J. Hogan, C. L. Haynes, M. Garwood, and J. C. Bischof. Accounting for biological aggregation in heating and imaging of magnetic nanoparticles. *Tecnology*, 23:214–228, 2014.
- [24] R. Di Corato, A. Espinosa, L. Lartigue, M. Tharaud, S. Chat, T. Pellegrino, C. Mnager, F. Gazeau, and C. Wilhelm. Magnetic hyperthermia efficiency in the cellular environment fordifferent nanoparticle designs. *Biomaterials*, 35:6400–6411, 2014.
- [25] I. Andreu, E. Natividad, L. Solozbal, and O. Roubeau. Nano-objects for addressing the control of nanoparticle arrangement and performance in magnetic hyperthermia. *ACS nano*, 9:1408–1419, 2015.
- [26] E. Alphandry, S. Faure, O. Seksek, F. Guyot, and I. Chebbi. Chains of magnetosomes extracted from amb-1 magnetotactic bacteria for application in alternative magnetic field cancer therapy. *ACS nano*, 5:6279–96, 2011.
- [27] M. S. Carrio, V. R. R. Aquino, G. T. Landi, E. L. Verde, M. Sousa, and A. F. Bakuzis. Giant-spin nonlinear response theory of magnetic nanoparticle hyperthermia: A field dependence study. *Journal of Applied Physics*, 121:173901, 2017.
- [28] A. Donev, i. Cisse, D. Sachs, E. A. Variano, F. H. Stillinger, R. Connelly, S. Torquato, and P.M. Chaikin. Improving the density of jammed disordered packings using ellipsoids. *Science*, 303:990–993, 2004.
- [29] H. B. Callen and E. Callen. The present status of the temperature dependence of magnetocrystalline anisotropy, and the $l(l+1)^2$ power law. *J. Phys. Chem. Solids*, 27:1271–1285, 1966.
- [30] B. Gleich and J. Weizenecker. Tomographic imaging using the nonlinear response of magnetic particles. *Nature*, 435:1214–1217, 2005.

- [31] P. W. Goodwill, E. U. Saritas, L. R. Croft, T. N. Kim, K. M. Krishnan, D. V. Schaffer, and S. M. Conolly. X-space mpi: Magnetic nanoparticles for safe medical imaging. *Advanced Materials*, 24:3870–3877, 2012.
- [32] J. B. Weaver, A. M. Rauwerdink, and E. W. Hansen. Magnetic nanoparticle temperature estimation. *Medical Physics*, 36(5):1822–1829, 2009.
- [33] J. Zhong, W. Liu, L. Kong, and P. C. Morais. A new approach for highly accurate, remote temperature probing using magnetic nanoparticles. *Scientific Reports*, 4:6338, 2014.
- [34] W. C. Nunes, W. S. D. Folly, P. J. Sinnecker, and M. A. Novak. Temperature dependence of the coercive field in single-domain particle systems. *Physical Review B*, 70:014419, 2004.
- [35] J. Rivas J. Garcia-Otero, A. J. Garcia-Bastida. Influence of temperature on the coercive field of non-interacting fine magnetic particles. *J. Magn. Magn. Mater.*, 189:377–383, 1998.
- [36] K. Byrappa and M. Yoshimura. *Handbook of hydrothermal technology*. Elsevier, 2001.
- [37] M. H. Sousa, G. J. da Silva, J. Depeyrot, F. A. Tourinho, and L. F. Zara. Chemical analysis of size-tailored magnetic colloids using slurry nebulization in icp-oes. *Microchemical Journal*, 97(2):182–187, 2011.
- [38] R. Massart, V. Dubois, E. Cabuil, and E. Hasmonay. Preparation and properties of monodisperse magnetic fluids. journal of magnetism and magnetic materials. *J. Magn. Magn. Mater.*, 149:1–5, 1995.
- [39] A. F. Bakuzis and P. C. Morais. On the origin of the surface magnetic anisotropy in manganese-ferrite nanoparticles. *J. Magn. Magn. Mater.*, 226-230:1924–1926, 2001.
- [40] M. T. A. Eloi, J. L. Santos, P. C. Morais, and A. F. Bakuzis. Field-induced columnar transition of biocompatible magnetic colloids: An aging study by magnetotransmissivity. *Physical Review E*, 82:021407, 2010.
- [41] M. Klokkenburg, B. H. Ern e, J. D. Meeldijk, A. Wiedenmann, A. V. Petukhov, R. P. A. Dullens, and A. P. Philipse. In situ imaging of field induced hexagonal columns in magnetite ferrofluids. *Phys. Rev. Lett.*, 97:185702, 2006.
- [42] E. S. Gonalves, D. R. Cornejo, C. L. P. Oliveira, A. M. Figueiredo Neto, J. Depeyrot, F. A. Tourinho, and R. Aquino. Magnetic and structural study of electric double-layered ferrofluid with $\text{MnFe}_2\text{O}_4@ \gamma - \text{Fe}_2\text{O}_3$ nanoparticles of different mean diameters: Determination of the magnetic correlation distance. *Phys. Rev. E*, 91:042317, 2015.